Supporting Information

Shell structure, magnetic and magnetodynamic properties of oxidized iron nanoparticles with partial gold coating

Sergey Lyaschenko[1,*], Ivan Tarasov[1], Tatyana Andryushchenko[1,2], Ivan Yakovlev[1], Dmitry Velikanov[1], Mikhail Volochaev[1,2], Ivan Nemtsev[1,2], Ruslan Kriukov[3], Olga Maximova[1,*], Dmitry Shevtsov[1], Sergey Varnakov[1,2], Sergei Ovchinnikov[1]

1 Kirensky Institute of Physics, Federal Research Center KSC SB RAS, Krasnoyarsk, 660036 Russia
2 Krasnoyarsk Scientific Center, Federal Research Center KSC SB RAS, Krasnoyarsk, 660036 Russia
3 National Research Lobachevsky State University of Nizhny Novgorod, Nizhny Novgorod, 603022 Russia

*E-mail: lsa@iph.krasn.ru, maximo.a@mail.ru

Experimental details

1. Samples synthesis. Characterization by scanning (SEM) and transmission electron microscopy (TEM)

The samples were synthesized by ultra-high vacuum (UHV) thermal deposition of high-purity iron (99.99%) onto an atomically pure NaCl(100) surface cleaved in air and annealed in UHV at room temperature (RT). The base pressure in the technological UHV chamber is ~10^{-7} Pa. Film homogeneity was additionally ensured by axial rotation of the substrate during deposition. The integral thickness of the iron layer in terms of the standard bulk density ρ_{Fe} 7.87 g/cm^3 for samples was (2.8 ± 0.1) nm. To start the nucleation process (surface nucleation of NPs), the samples were briefly annealed at UHV up to 750 K, with the sample surface being monitored by reflected high-energy electron diffraction. After UHV annealing of the iron film, type A samples were extracted from the UHV. On the surface of the type B sample a (1.1 ± 0.1) nm layer of high-purity gold (99.999%) (standard density 19.3 g/cm^3) was thermally deposited at RT. The technological thickness of the metals was set by the deposition time at a known rate. The deposition rate was calibrated by the X-ray fluorescence method and TEM of calibration epitaxial films.

SEM analysis was carried out using a Hitachi S5500 scanning electron microscope. TEM of the samples was performed on Hitachi HT7700 microscope equipped with selected area electron diffraction (SAED) spectrometer 6T/60 Bruker.

2. SAED analysis of hydrated samples

The selected area electron diffraction experiment was performed at a constant camera length in diffraction mode of HT7700 microscope. The intensity profiles were produced using CrysTBox [1]. To perform a qualitative and quantitative analysis of the intensity profiles, we used Rietveld refinement with Pseudo-Vogt peak profiles. Temperature factors were not taken into account, since weak and broad reflections corresponded to the iron oxides/hydroxides.

Rietveld refinement of the intensity profile of the SAED pattern for the oxidized NPs of sample A-III showed that the most accurate correspondence of the theoretical and experimental profiles is observed for three phases γ-Fe$_2$O$_3$, Fe$_3$O$_4$, α-FeO(OH) with R$_{wp}$ equal to 35.33, 33.46, 36.30 %, respectively (Table S2, Fig. S3). However, the misfit between α-FeO(OH) lattice parameters fitted and those available in the literature is as big as -47.1 %, which indicates that this phase cannot be considered as a primary phase formed during the oxidation of the iron NPs. In turn, the misfits of the γ-Fe$_2$O$_3$, Fe$_3$O$_4$ are much lower and lie in the range of possible values within 10 % [2]. However, the obtained value is relatively high, which confirms the fact that the oxide shell formed is strongly strained to be correct. For instance, a probable candidate for an orientation relationship for an alignment of the γ-Fe$_2$O$_3$ oxide shell on the iron core could be Fe{011}<022>//γ-Fe$_2$O$_3${004}<100> with the interplanar and interatomic spacing misfits of 2.74 and -2.82 %, respectively. This indicates a relatively high error in the calibration procedure based on the carbon supporting film diffraction pattern. In the case of broad diffraction peaks for 2-10 nm iron oxide particles the precise determination of the peak center for the carbon supporting film does not seem

achievable. Rough estimation of possible correspondence of Fe(110) plane to the reflection around 2θ equal to $0.8°$ (Fig. S4) gives the misfit value for bcc-Fe lattice of -10.98 %, which shows a negative value, as in the case of γ-Fe$_2$O$_3$, Fe$_3$O$_4$. The difference between the misfit value for iron and Fe$_3$O$_4$ unit cell fitted is comparable to the estimated value for the Fe{011}<022>//γ-Fe$_2$O$_3${004}<100> orientation relationship.

Thus, we carried out an additional refinement of the intensity profile of the SAED pattern for the oxidized NPs of sample A-III for three compounds (γ-Fe$_2$O$_3$, Fe$_3$O$_4$, α-FeO(OH)) taking into consideration possible changes in the occupancies of atomic positions of the oxide phases. The refinement results in lower R_{wp} for the γ-Fe$_2$O$_3$, Fe$_3$O$_4$ phases (23.77 and 22.99 %, respectively). In the case of the α-FeO(OH) phase, the refinement quality remains almost identical (R_{wp} = 34.98 %) to the previous fitting procedure (Table S2). Thus, taking into account the analysis of the contrast between the nanoparticle core and shell discussed above, i.e. the iron density, we can conclude the primary compound tended to form during the oxidation process is γ-Fe$_2$O$_3$. Even though the γ-Fe$_2$O$_3$, Fe$_3$O$_4$ compound show almost identical electron diffraction pattern and may differ by the lattice parameter, which is not resolved in the case of the electron diffraction technique for particles with an average diameter of 2-10 nm. In such a situation when two phases γ-Fe$_2$O$_3$, Fe$_3$O$_4$ are present, there is an overlap of broad reflection peaks from each phase.

In addition, one can notice the presence of the diffraction peak around $1.05°$ on the intensity profile for samples A-III and B-III (Fig. 6), which cannot be described by the γ-Fe$_2$O$_3$ or Fe$_3$O$_4$ compounds. However, it may correspond to the α-FeO(OH)(410) or (302) planes with higher intensity caused by lattice defects and the texturing.

3. Ion etching photoelectron spectroscopy (XPS) of hydrated samples

XPS analysis was carried out on an Omicron Multipobe RM UHV complex with monochromatic Mg Kα x-ray sources and a hemispherical energy analyzer. The sample was placed perpendicular to the direction of the energy analyzer, at an angle of 45° to the X-ray source. To remove contaminants and profile the sample in depth, ion etching was used at a rate of 0.15-0.18 nm/min. An ion beam with a current density of 0.7 μA/cm^2 and a diameter of 20 mm was directed at an angle of 45° to the surface of the stationary sample. The etching rate was calibrated using Co/Pt metal films and TiO$_x$ films, and the same values were obtained when analyzing GaAs. The spectra were recorded with a step of 0.2 eV at a base pressure in the chamber of ~10^{-7} Pa. Photoelectrons were collected from a region with a diameter of about 3 mm in the center of the etching crater. The energy spectra were calibrated using the C1s peak at 284.75 eV. XPS data analysis was performed using the Spectra Data Processor (SDP v.8.0) (https://xpslibrary.com/, USA). All peaks were fitted with 100% Gaussians, and background was subtracted using the standard Shirley method.

4. Magnetic properties

The field dependences of magnetization $M(H)$ were measured using vibration magnetometry (VSM) at room temperature. Temperature dependences of magnetization $M(T)$ were obtained using superconducting quantum interference device (SQUID) magnetometer. To increase the magnetic signal,

powder samples were prepared by mechanically removing a layer of particles from the surface of the NaCl substrate in air and then pouring them into the measuring cell of the magnetometer. The paramagnetic and diamagnetic contributions from magnetic impurities in the measuring cell and substrate residues were subtracted from the original data. Magnetization is recalculated to the mass of pure iron. The measured data were smoothed by the Savitzky-Golay method and approximated by the least squares method in Origin software (OriginLab Corporation, USA).

5. Magnetodynamics of water-dispersed particles

The solution for single-wavelength reflection ellipsometry (SWE) analysis was prepared by ultrasonic destruction of a monolayer of sample B-III particles in a 0.01 mM aqueous solution of citric acid for 3 minutes in a quartz beaker at RT. Within five minutes after turning off the ultrasound, the resulting solution was poured into a sealed measuring cell of a polylactide ellipsometer, the surface of the solution was leveled with a microdoser to adjust the measuring circuit of the ellipsometer, and the solution was held to establish equilibrium between the vapor and liquid in the cell. Measurements were carried out at 25°C and relative humidity close to 100%. For ellipsometric measurements, a spectral ellipsometer Ellips-1891 (Russia) was used in the mode of single-wave measurements versus time. The wavelength was 555 nm, the angle of incidence of light was 50.6° to the normal of the solution surface, which is close to the Brewster angle of the air/water interface (53.123°). The recording mode for ellipsometric angles Ψ and Δ was continuous. In this case, a cylindrical NdFeB permanent magnet was periodically applied to the solution surface through the light-proof plastic wall of the cell, creating a magnetic field gradient of 400 Oe/mm in the cuvette with the solution, orthogonal to the solution surface. An elliptical-shaped spot of an ellipsometric beam with dimensions of 2x4 mm and a permanent magnet diameter of 6 mm provide a magnetic gradient inhomogeneity of ± 10% within the measured surface area. The magnitude of the magnetic field at the air/liquid interface on the central axis of the magnet is 1.4 kOe. The magnet was quickly (less than a second) brought to the solution, and after 200 seconds it was quickly moved away from the solution for 200 seconds. The polarity of the field did not change. The procedure was repeated five times in a row with continuous SWE recording.

Table S1. Iron density in known oxides, hydroxides and oxyhydroxides. Calculated values are marked with *.

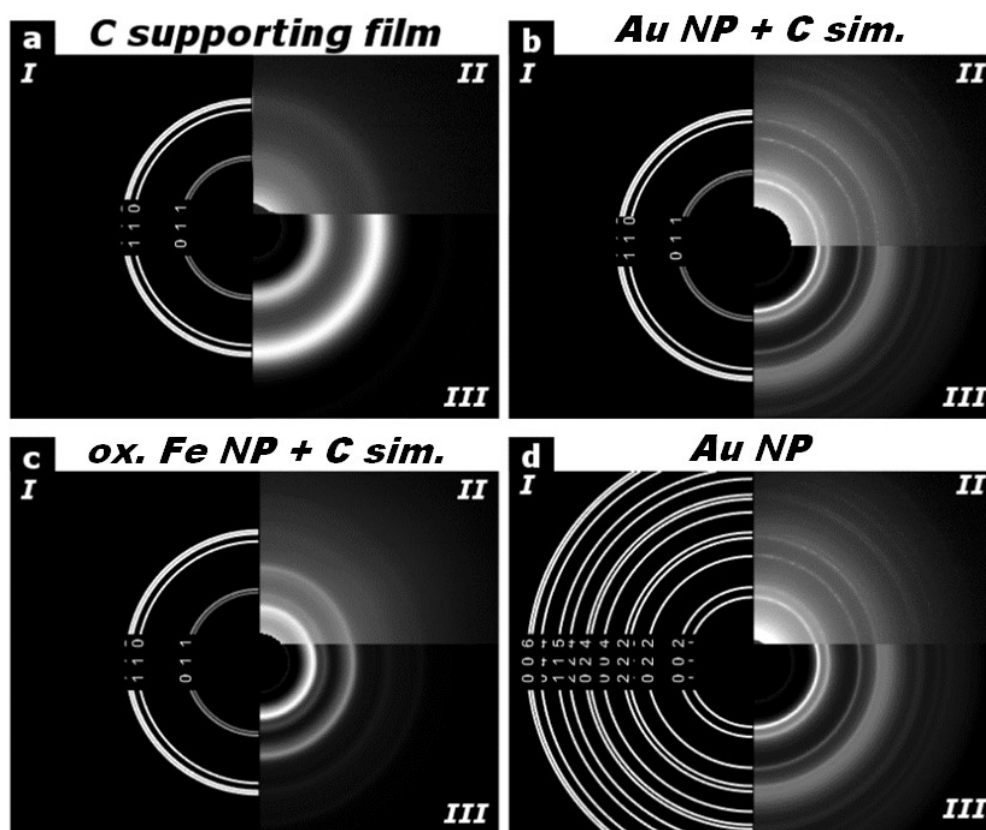| Chemical compound, symmetry, space group	Full density ρ_Σ, g/cm^3	Full molecular weight M_Σ, g/mol	Iron molar weight $M_{Fe} \cdot n_{Fe}$, g/mol	Iron density $\rho_\Sigma \cdot M_{Fe} \cdot n_{Fe} / M_\Sigma$, g/cm^3
FeO(OH), α-FeO(OH) (III) orthorhombic, Pnma [3]	4.28	88.9	56	2.69
FeO(OH), β-FeO(OH) tetragonal, I4/m [4]	3.45	88.9	56	2.17
FeO(OH), γ-FeO(OH) (III) orthorhombic, Cmcm [5]	4.06	88.9	56	2.56
FeO(OH), ε-FeO(OH) (III) orthorhombic, P2$_1$nm [6]	4.44*	88.9	56	2.80*
FeO(OH), δ-FeO(OH) (III) hexagonal, P3m1 [7, 8]	3.75, 4.3*	88.9	56	2.36, 2.7*
Fe(OH)$_2$, hexagonal, P$\bar{3}$m1 [9]	3.65*	89.9	56	2.28*
Fe(OH)$_3$, orthorhombic Pmmn [10]	3.32, 3.35*	106.9	56	1.74, 1.76*
Fe$_2$O$_3$, α-Fe$_2$O$_3$ (III) trigonal, R$\bar{3}$c [11]	5.14, 5.28*	159.7	112	3.6, 3.7*
Fe$_2$O$_3$, β-Fe$_2$O$_3$ (III) cubic, Ia$\bar{3}$ [12, 13]	5.14*	159.7	112	3.16*
Fe$_2$O$_3$, γ-Fe$_2$O$_3$ (III) cubic spinel, Fd$\bar{3}$m [14, 15]	4.86, 5.49*	159.7	112	3.4, 3.85*
Fe$_2$O$_3$, ε-Fe$_2$O$_3$ (III) orthorhombic, Pna2$_1$ [16, 17]	4.73, 5.08*	159.7	112	3.32, 3.56*
Fe$_3$O$_4$, cubic Fd$\bar{3}$m [18, 19]	5.2	231.5	168	3.77
FeO, cubic Fm$\bar{3}$m [20, 21]	5.6, 6.02*	71.8	56	4.3, 4.7*

Figure S1. Electron diffraction pattern obtained for: (a) carbon supporting film; (b, d) Au NPs (~ 10 nm diameter) on a carbon supporting film; (c) oxidized NPs of sample A-III, where "I" corresponds to the theoretical pattern; "II" is an original diffraction image, and "III" is a SAED pattern with background subtraction.
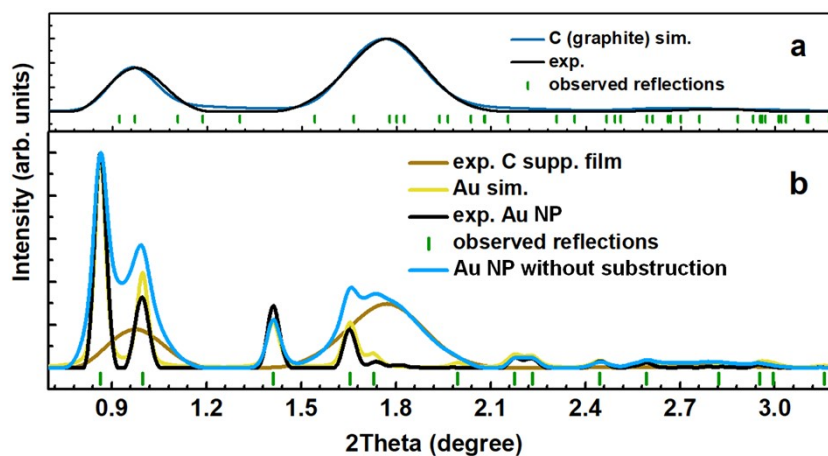
Figure S2. (a) Experimental and simulated SAED intensity profiles for the carbon supporting film; (b) experimental and simulated SAED intensity profiles for Au NPs (~ 10 nm diameter), experimental SAED intensity profiles for the carbon supporting film is also given for illustration.
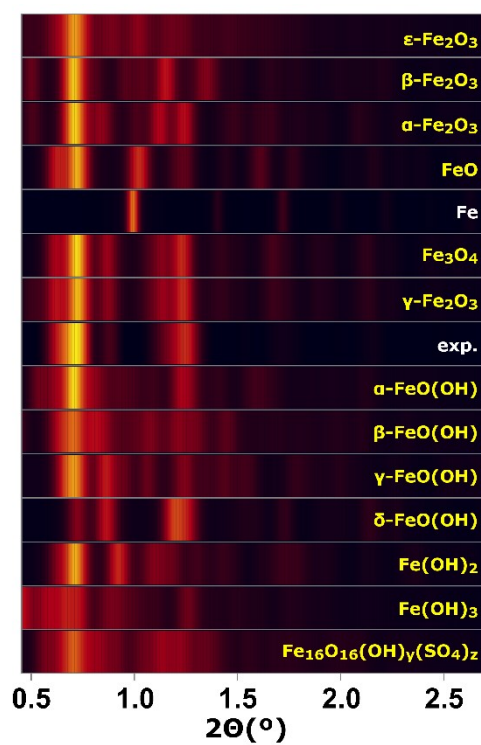
Figure S3. Experimental SAED intensity profiles of the oxidized NPs along with simulated powder profiles corresponding to the indicated phase.

Table S2. Refinement results for the lattice parameters (oxidized NPs)

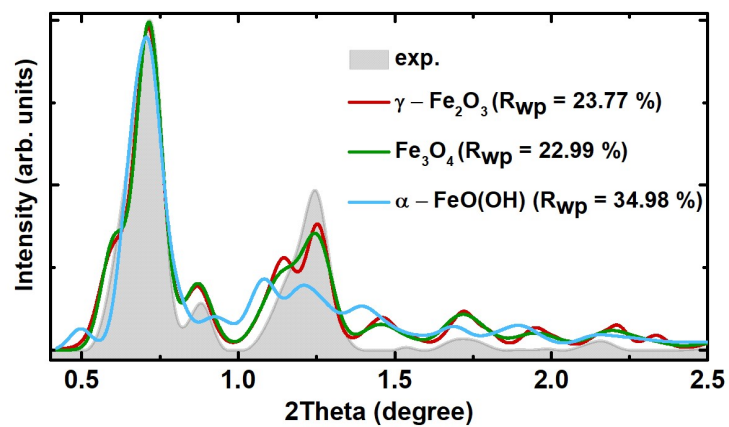| Ref.	Phase		Lattice parameters, Å		Misfit, %	R_wp, %
			Fitted	Literature		
[22]	**C**	*a, b*	fixed	2.47	-	9.77
		c	fixed	6.79	-	
[23]	**Au**	*a, b,c*	4.034	4.072	0.932	17.02
[24]	**Fe**	*a, b,c*	3.22	2.8665	-10.98	98.89
[25]	**α-Fe₂O₃**	*a, b*	5.608	5.03	-10.3	42.41
		c	14.034	13.75	-2.02	
[26]	**β-Fe₂O₃**	*a, b,c*	9.87	9.4	-4.72	54.54
[27]	**γ-Fe₂O₃**	*a, b,c*	9.207	8.34	-9.46	35.33
[28]	**ε-Fe₂O₃**	*a*	5.563	5.09	-8.59	47.69
		b	11.03	8.77	-20.5	
		c	8.415	9.47	12.51	
[29]	**Fe₃O₄**	*a, b,c*	9.253	8.4	-9.23	33.46
[30]	**FeO**	*a, b,c*	5.573	4.3	-22.8	50.30
[31]	**α-FeO(OH)**	*a*	9.975	9.951	-0.24	36.30
		b	5.697	4.598	-23.9	
		c	3.466	3.018	-14.8	
[32]	**β-FeO(OH)**	*a*	10.05	10.6	5.347	50.30
		b	3.723	3.03	-18.6	
		c	9.124	10.5	15.24	
[24]	**γ-FeO(OH)**	*a*	16.9	12.4	-26.6	49.12
		b	3.214	3.87	20.42	
		c	3.236	3.06	-5.43	
[33]	**δ-FeO(OH)**	*a, b*	3.214	2.95	-8.22	75.53
		c	4.247	4.56	7.378	
[24]	**Fe(OH)₂**	*a, b*	3.702	3.26	-12	51.89
		c	5.949	4.61	22.6	
[34]	**Fe(OH)₃**	*a*	13.48	7.54	-44	67.20
		b	13.57	7.56	-44.3	
		c	13.47	7.56	-43.9	
[35]	**Fe₁₆O₁₆(OH)ᵧ(SO₄)_z**	*a*	9.772	10.8	10.74	51.81
		b	7.107	6	-15.6	
		c	7.107	10.5	47.93	

Figure S4. Experimental and simulated SAED intensity profiles for the oxidized NPs of sample A-III
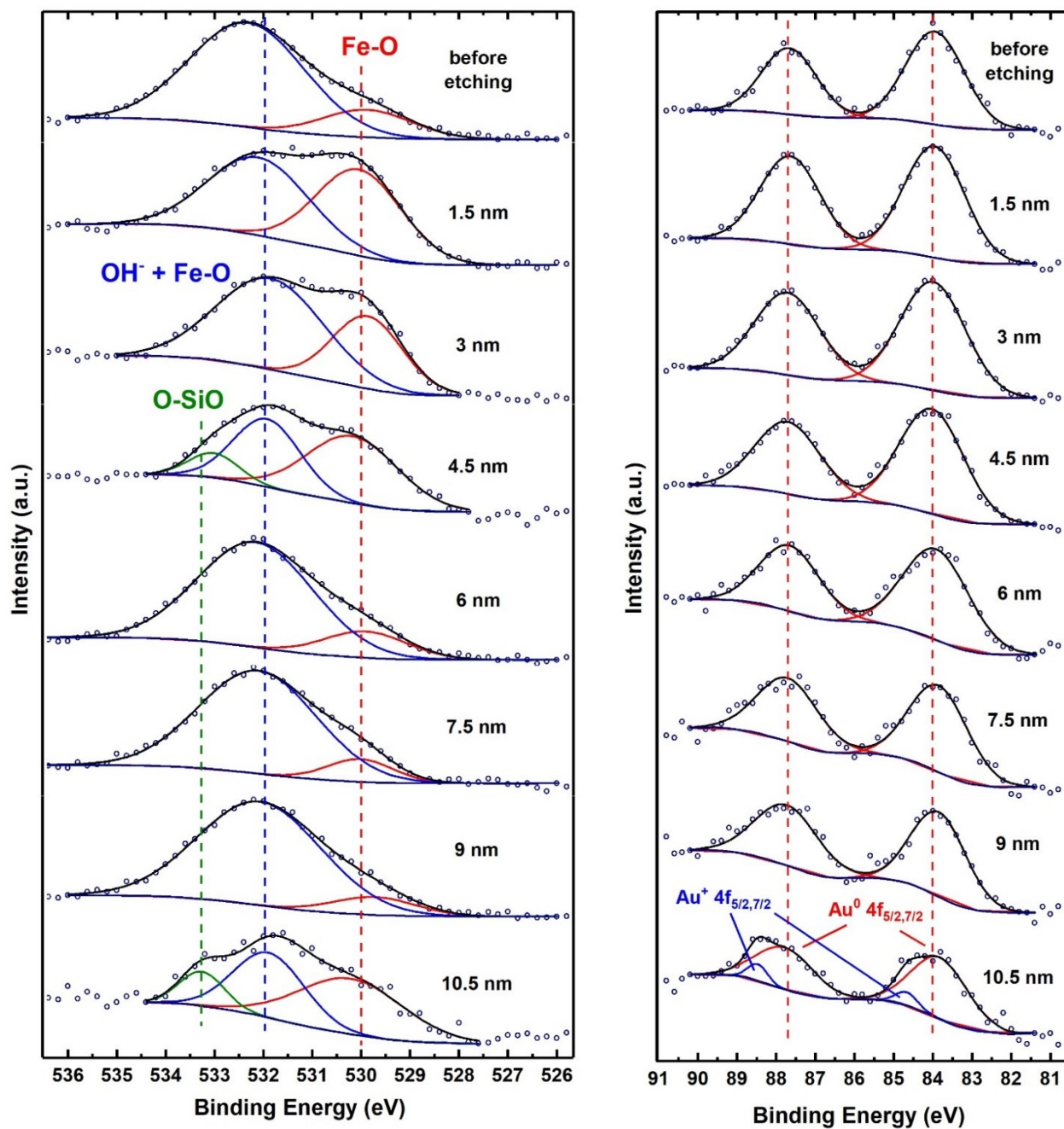
Figure S5. XPS O1s (left) and Au4f (right) spectra for sample B-III on a quartz substrate before and after etching
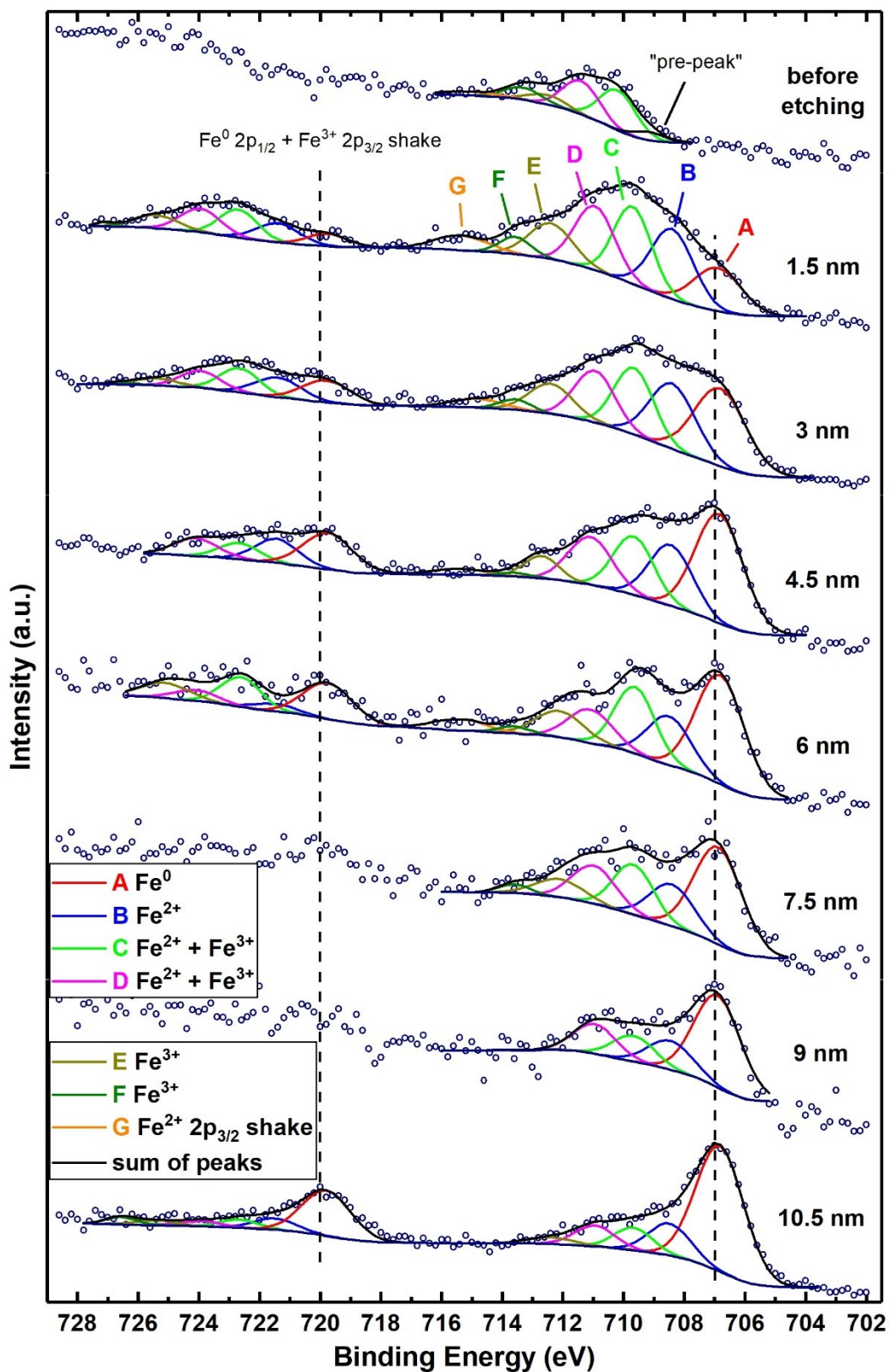
Figure S6. XPS Fe2p spectra for sample B-III on a quartz substrate before and after etching

Supplementary references

[1] M. J. Klinger, *Appl. Crystallogr.*, 2017, **50** (4), 1226–1234.

[2] S. R. Singamaneni, J. T. Prater, J. Narayan, *Appl. Phys. Rev.*, 2016, **3** (3), 031301.

[3] H. Yang, R. Lu, R. T. Downs, G. Costin, *Acta Crystallographica Section E*, 2006, **62**(12), 250–252.

[4] A. Szytula, M. Balanda, Ž Dimitrijevi, *Physica Status Solidi (a)*, 1970, **3**(4), 1033–1037.

[5] A. Oleś, A. Szytuła, A. Wanic, *Physica Status Solidi (b)*, 1970, **41**(1), 173–177.

[6] N. B. Bolotina, V. N. Molchanov, T. I. Dyuzheva, L. M. Lityagina, N. A. Bendeliani, *Crystallography Reports*, 2008, **53**, 960–965.

[7] Sh. Okamoto, Structure of δ-FeOOH, *J. of the American Cer. Soc.*, 1968, **51**(10), 594–598.

[8] A. Ya. Vlasov, M. N. Rukosuev, *Soviet Phys. J.*, 1972, **15**, 1226–1229.

[9] H. Miyamoto, *Materials Research Bulletin*, 1976, **11**(3), 329-335.

[10] C. A. McCammon, A. Pring, H. Keppler, T. Sharp, *Phys. Chem. Minerals*, 1995, **22**, 11–20.

[11] R. Przeniosło, I. Sosnowska, M. Stękiel, D. Wardecki, A. Fitch, J. B. Jasiński, *Phys. B: Cond. Matter*, 2014, **449**, 72–76.

[12] T. Danno, D. Nakatsuka, Y Kusano, H. Asaoka, M. Nakanishi, T. Fujii, Y. Ikeda, J. Takada, *Cryst. Growth Des.*, 2013, **13**(2), 770–774.

[13] L. Ben-Dor, E. Fischbein, Z. Kalman, *Acta Cryst. Sec. B Struc. Cryst. and Crystal Chem.*, 1976, **32**(2), 667–667.

[14] G. Ennas, G. Marongiu, A. Musinu, A. Falqui, P. Ballirano, R. Caminiti, *J. of Materials Research*, 1999, **14**(15), 1570–1575.

[15] E Tronc, A Ezzir, R Cherkaoui, C Chanéac, M Noguès, H Kachkachi, D Fiorani, A.M Testa, J.M Grenèche, J.P Jolivet, *J. of Magnetism and Magnetic Materials*, 2000, **221**(1–2), 63–79.

[16] Sh. Sakurai, A. Namai, K. Hashimoto, Sh. Ohkoshi, *J. Am. Chem. Soc.*, 2009, **131**(51), 18299–18303.

[17] K. Kelm, W. Mader, *Zeitschrift für anorganische und allgemeine Chemie*, 2005, **631**(12), 2383–2389.

[18] M. E. Fleet, *Acta Cryst.*, 1984, **40**, 1491–1493.

[19] S. Upadhyay, K. Parekh, B. Pandey, *J. of Alloys and Comp.*, 2016, **678**, 478–485.

[20] F. Schrettle, Ch. Kant, P. Lunkenheimer, F. Mayr, J. Deisenhofer, A. Loidl, *The Euro. Phys. J. B*, 2012, **85**, 164.

[21] R. Tanaka, T. Sakamaki, E. Ohtani, H. Fukui, S. Kamada, A. Suzuki, S. Tsutsui, H. Uchiyama, A. Q. R. Baron, *Prog Earth Planet Sci*, 2020, **7**, 23.

[22] O. Hassel, H. Mark, *Zeitschrift für Phys.*, 1924, **25** (1), 317–337.

[23] I.-K. Suh, H. Ohta, Y. J. Waseda, *Mater. Sci.,* 1988, **23** (2), 757–760.

[24] R. W. G. Wyckoff, *Crystal Structures, Second edition*, Interscience Publishers, New York, 1963.

[25] Y. El Mendili, J.-F. Bardeau, N. Randrianantoandro, F. Grasset, J.-M. Greneche, *J. Phys. Chem. C*, 2012, **116** (44), 23785–23792.

[26] T. Danno, D. Nakatsuka, Y. Kusano, H. Asaoka, M. Nakanishi, T. Fujii, Y. Ikeda, J Takada, *Cryst. Growth Des.*, 2013, **13** (2), 770–774.

[27] E. Solano, C. Frontera, T. Puig, X. Obradors, S. Ricart, J. Ros., *J. Appl. Crystallogr.*, 2014, **47** (1), 414–420.

[28] M. Gich, C. Frontera, A. Roig, E. Taboada, E. Molins, H. R. Rechenberg, J. D. Ardisson, W. A. A. Macedo, C. Ritter, V. Hardy, J. Sort, V. Skumryev, J. Nogués, *Chem. Mater.,* 2006, **18** (16), 3889–3897.

[29] F. F. Ferreira, E. Granado, W. Carvalho Jr, S. W. Kycia, D. Bruno, R. Droppa Jr, *J. Synchrotron Radiat.*, 2006, **13** (1), 46–53.

[30] R. W. G. Wyckoff, E. D. Crittenden, *Zeitschrift für Krist. - Cryst. Mater.,* 1926, **63** (1–6), 507-537.

[31] F. Alessandro, P. V. Gualtieri, *Am. Mineral.*, 1999, **84** (5–6), 895–904.

[32] J. E. Post, P. J. Heaney, R. B. Von Dreele, J. C. Hanson, *Am. Mineral.*, 2003, **88** (5–6), 782–788.

[33] G. Patrat, F. de Bergevin, M. Pernet, J. C. Joubert, *Acta Crystallogr. Sect. B Struct. Sci.,* 1983, **39** (2), 165–170.

[34] W. D. Birch, A. Pring, A. Reller, H. W. Schmalle, *Am. Mineral.,* 1993, **78** (7–8), 827–834.

[35] Fernandez-Martinez, A.; Timon, V.; Roman-Ross, G.; Cuello, G. J.; Daniels, J. E.; Ayora, C. *Am. Mineral.*, 2010**, 95** (8–9), 1312–1322.